Challenges in Drift-Diffusion Semiconductor Simulations

Patricio Farrell and Dirk Peschka

Abstract We study and compare different discretizations of the van Roosbroeck system for charge transport in bulk semiconductor devices that can handle nonlinear diffusion. Three common challenges corrupting the precision of numerical solutions will be discussed: boundary layers, discontinuities in the doping profile, and corner singularities in L-shaped domains. The most problematic of these challenges are boundary layers in the quasi-Fermi potentials near ohmic contacts, which can have a drastic impact on the convergence order.

Keywords Finite volume method · Finite element method · Nonlinear diffusion · Scharfetter-gummel scheme · Semiconductors · Van roosbroeck system · Convergence order · Diffusion enhancement

MSC (2010) 35Q99 · 82D37 · 65M08 · 65M06 · 65M60

1 Introduction

The present paper aims at comparing different discretization philosophies for semiconductor problems. We study three major challenges for recent finite element and finite volume schemes which are designed to deal with nonlinear diffusion in a thermodynamic consistent way and are based on quasi-Fermi potentials as primary variables. In particular, we study the error and convergence rate of the numerical solutions in the presence of: boundary layers, discontinuous doping profile and corner singularities.

P. Farrell (✉) · D. Peschka
Weierstrass Institute (WIAS), Mohrenstr. 39, 10117 Berlin, Germany
e-mail: patricio.farrell@wias-berlin.de

D. Peschka
e-mail: dirk.peschka@wias-berlin.de

R. Klöfkorn et al. (eds.), *Finite Volumes for Complex Applications IX - Methods, Theoretical Aspects, Examples*, Springer Proceedings in Mathematics & Statistics 323,
https://doi.org/10.1007/978-3-030-43651-3_58

2 Modelling Semiconductors with Ohmic Contacts

2.1 Stationary van Roosbroeck System

The van Roosbroeck system is a drift-diffusion model, which describes the recombination and transport of charge carriers driven by diffusion and by electric fields within a semiconductor device. It consists of three nonlinear, coupled partial differential equations for the electrostatic potential $\psi : \Omega \to \mathbb{R}$ as well as the non-negative electron and hole densities $n : \Omega \to \mathbb{R}^+$ and $p : \Omega \to \mathbb{R}^+$, namely a Poisson equation and two continuity equations. We consider a homogeneous material and some domain $\Omega \subseteq \mathbb{R}^d$ for $d \in \{1, 2, 3\}$ in an isothermal setting. Then the stationary van Roosbroeck system is given by the system of elliptic partial differential equations

$$-\nabla \cdot (\varepsilon_0 \varepsilon_r \nabla \psi) = q\left(C + p(\psi, \varphi_p) - n(\psi, \varphi_n)\right), \tag{1a}$$

$$\nabla \cdot \mathbf{j}_n = +qR, \tag{1b}$$

$$\nabla \cdot \mathbf{j}_p = -qR, \tag{1c}$$

where q denotes the elementary charge, ε_0 is the vacuum permittivity and ε_r is the relative permittivity of the material. The recombination rate R and the charge-carrier currents $\mathbf{j}_n, \mathbf{j}_p$ depend on the solution n, p, ψ and vanish in thermal equilibrium. The given doping concentration $C : \Omega \to \mathbb{R}$ (intentionally introduced impurities) varies spatially and can have discontinuities. The equations of state are given by

$$n(\psi, \varphi_n) = N_c \mathscr{F}\left(\frac{q(\psi - \varphi_n) - E_c}{k_B T}\right), \tag{2a}$$

$$p(\psi, \varphi_p) = N_v \mathscr{F}\left(\frac{q(\varphi_p - \psi) + E_v}{k_B T}\right), \tag{2b}$$

where the statistical distribution function $\mathscr{F}$ relates the electron and hole densities n, p to the quasi-Fermi potentials φ_n, φ_p. Working with quasi-Fermi potentials has all the advantages mentioned in the introduction, in particular from a modeling and computational point of view. Furthermore, we set the recombination rate to zero as it plays a minor role for most of our considerations.

The effective density of states for electrons in the conduction band N_c and holes in the valence band N_v as well as the corresponding band-edge energies E_c, E_v and the band gap $E_g = E_c - E_v$ are material parameters and assumed to be spatially constant in this paper. Temperature and the Boltzmann constant are denoted with T and k_B. The three most important reference cases for the statistical distribution functions are the Boltzmann, Blakemore and Fermi-Dirac function. For each distribution function, the corresponding current densities in (1b) and (1c) are

$$\mathbf{j}_n = -q\mu_n n\nabla\varphi_n = -q\mu_n n\nabla\psi + qD_n\nabla n, \tag{3a}$$
$$\mathbf{j}_p = -q\mu_p p\nabla\varphi_p = -q\mu_p p\nabla\psi - qD_p\nabla p. \tag{3b}$$

Using the thermal voltage $U_T = \frac{k_B T}{q}$, the diffusion coefficients D_n, D_p are linked to the carrier mobilities μ_n, μ_p via generalized Einstein relations

$$\frac{D_n}{\mu_n} = U_T\, g\big(\eta_n\big), \qquad \frac{D_p}{\mu_p} = U_T\, g\big(\eta_p\big), \qquad g(\eta) = \frac{\mathscr{F}(\eta)}{\mathscr{F}'(\eta)}, \tag{4}$$

where g is the diffusion enhancement as motivated in [8].

The system (1) is supplied with mixed Dirichlet-Neumann boundary conditions.

3 Discretization of the van Roosbroeck System Using Potentials

In the following we are going to explain standard discretization methods to solve the van Roosbroeck system.

3.1 Finite Element Method

Assume $\Omega \subset \mathbb{R}^2$ is a polygonal domain and let $\mathscr{T}_h$ be an admissible decomposition of Ω into N_{tria} triangles and N_{vert} vertices, such that $\Omega = \bigcup_{t=1}^{N_{\text{tria}}} \tau_t$ for $\tau_t \in \mathscr{T}_h$. Similar as in [2], we solve the stationary van Roosbroeck system (1) using a standard P_1 finite element method. We seek the electrostatic potential and the quasi-Fermi potentials $\mathbf{u}^h = (\psi^h, \varphi_n^h, \varphi_p^h) \in V^h$, such that the van Roosbroeck system can be written in the weak form as

$$0 = \int_\Omega \Big(\varepsilon_0\varepsilon_r \nabla\psi^h \cdot \nabla v_i - q\big(C + p(\psi^h, \varphi_p^h) - n(\psi^h, \varphi_n^h)\big)v_i\Big)\,\mathrm{d}x, \tag{5a}$$
$$0 = \int_\Omega \Big(q\mu_n n(\psi^h, \varphi_n^h)\nabla\varphi_n^h \cdot \nabla v_j - qR\left(n(\psi^h, \varphi_n^h),\, p(\psi^h, \varphi_p^h)\right) v_j\Big)\,\mathrm{d}x, \tag{5b}$$
$$0 = \int_\Omega \Big(q\mu_p p(\psi^h, \varphi_p^h)\nabla\varphi_p^h \cdot \nabla v_k + qR\left(n(\psi^h, \varphi_n^h),\, p(\psi^h, \varphi_p^h)\right) v_k\Big)\,\mathrm{d}x, \tag{5c}$$

for all suitable test functions $\mathbf{v}^h = (v_i, v_j, v_k) \in V^h$, where $V^h \cong \mathbb{R}^{N_{\text{vert}}\times 3}$ is the $3N_{\text{vert}}$ dimensional space of vectorial continuous functions which are piecewise linear on each triangle τ_t.

3.2 Finite Volume Method

In this section, we present a Voronoï finite volume technique [4, 6, 7]. Similar as for finite elements, we start by partitioning the domain Ω into non-intersecting, convex polyhedral control volumes ω_k such that $\Omega = \bigcup_{k=1}^{N_{\text{vert}}} \omega_k$. We associate with each control volume ω_k a node $\mathbf{x}_k \in \omega_k$. For every boundary intersecting control volume, we demand that this node lies on the boundary $\mathbf{x}_k \in \partial\Omega \cap \omega_k$. Assuming the partition is admissible [3], i.e. for two adjacent control volumes ω_k and ω_l, the edge $\overline{\mathbf{x}_k\mathbf{x}_l}$ of length h_{kl} is orthogonal to $\partial\omega_k \cap \partial\omega_l$, the normal vectors to $\partial\omega_k$ can be calculated by $\boldsymbol{\nu}_{kl} = (\mathbf{x}_l - \mathbf{x}_k)/\|\mathbf{x}_l - \mathbf{x}_k\|$. We note that the variables $(\psi, \varphi_n, \varphi_p)$ are of interest only at the nodes, not at the edges.

For each control volume ω_k, the finite volume discretization is given by the three equations:

$$\sum_{\omega_l \in \mathcal{N}(\omega_k)} |\partial\omega_k \cap \partial\omega_l| j_{\psi;k,l} = q|\omega_k| \left(C_k + p(\psi_k, \varphi_{p;k}) - p(\psi_k, \varphi_{n;k})\right), \tag{6a}$$

$$\sum_{\omega_l \in \mathcal{N}(\omega_k)} |\partial\omega_k \cap \partial\omega_l| j_{n;k,l} = +q|\omega_k| R(\psi_k, \varphi_{n;k}, \varphi_{p;k}), \tag{6b}$$

$$\sum_{\omega_l \in \mathcal{N}(\omega_k)} |\partial\omega_k \cap \partial\omega_l| j_{p;k,l} = -q|\omega_k| R(\psi_k, \varphi_{n;k}, \varphi_{p;k}). \tag{6c}$$

We denote with $\mathcal{N}(\omega_k)$ the set of all control volumes neighboring ω_k. In 2D, the measure $|\partial\omega_k \cap \partial\omega_l|$ corresponds to the length of the boundary line segment and in 3D to the area of the intersection of the boundary surfaces.

The unknowns $\psi_k, \varphi_{n;k}, \varphi_{p;k}$ correspond to the electrostatic potential as well as the quasi-Fermi potentials for electrons and holes evaluated at node $\mathbf{x}_k$. To approximate the fluxes in (6) using general $\mathscr{F}$, ideas from [1] are useful to derive a finite volume scheme for convection-diffusion problems in a *thermodynamically consistent* way by averaging the nonlinear diffusion term appropriately.

4 Numerical Examples

In this section, we are going to present numerical solutions of the van Roosbroeck system via FE and the Scharfetter-Gummel FV discretization. We focus on two challenges, which have an impact on the convergence rate of solutions: the size of a boundary layer and the regularity of the doping. Since in this section we are mostly concerned with numerical solutions, we will drop the superindex h. If necessary, we replace it with the acronym of the corresponding discretization method. Also we remind the reader that we solve the van Roosbroeck system without recombination, *i.e.*, $R \equiv 0$. Throughout this section, we use the Blakemore distribution function.

4.1 Resolution of Boundary Layer

In Fig. 1 the densities n, p and the doping C are shown for the two cases $\kappa = 5 \cdot 10^2$ and $\kappa = 5 \cdot 10^5$ at $V_{\text{ext}} = 3\,\text{V}$. Note that in both cases, the hole density p has a boundary layer at $x = 0$ and the electron density n has a boundary layer at $x = 0.3\,\mu\text{m}$. This boundary layer, however, is on the length scale of λ_D and therefore nicely resolved by the mesh. On the level of the plot, the difference in solutions corresponding to the two alternative doping profiles is not visible. In the left panel of Fig. 2 we show the potentials $(\psi, \varphi_n, \varphi_p)$ for $V_{\text{ext}} = 3\,\text{V}$. While the electrostatic potential in both cases is a rather smooth function (blue line), the quasi-Fermi potentials have a boundary layer of size ℓ_J (green and red line) that can not be resolved on any of the uniform meshes. This logarithmic boundary layer is predicted by our analysis in [5]. As one can see in Fig. 2 (middle and right panel), the solution effectively jumps within the last interval before the ohmic contact.

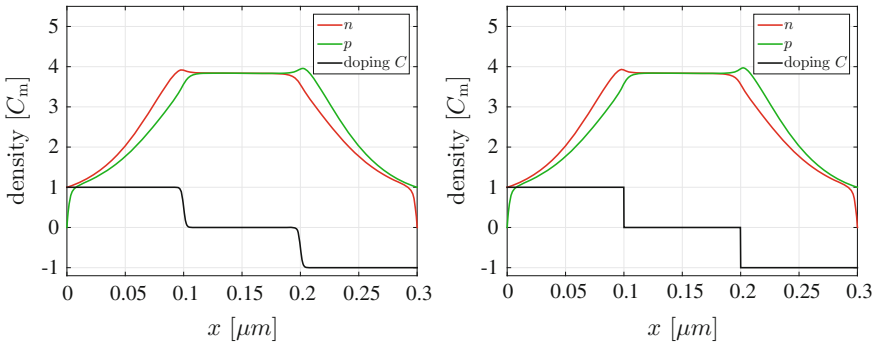

Fig. 1 1D electron and hole densities n, p and doping C at bias $V_{\text{ext}} = 3\,\text{V}$ shown (left) with $\kappa = 500$ and (right) with $\kappa = 5 \cdot 10^5$, the former yielding a smooth doping profile and the latter practically a discontinuous one

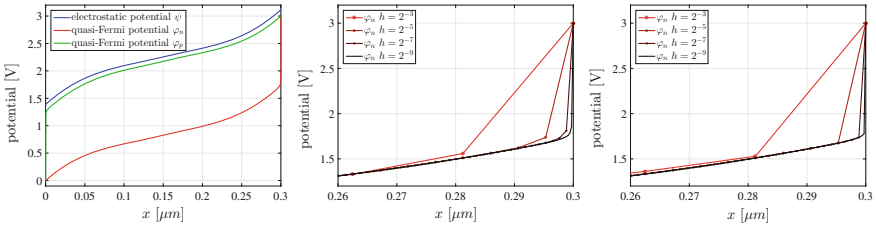

Fig. 2 1D quasi-Fermi potentials of electrons and holes φ_n, φ_p and electrostatic potential ψ (left) with bias $V_{\text{ext}} = 3\,\text{V}$ as well as boundary layers in the electron quasi-Fermi potential φ_n near $x = 0.3\,\mu\text{m}$ for different mesh resolutions h (middle) for finite element and (right) Scharfetter-Gummel type finite volume discretization for $\kappa = 500$

4.2 Regularity of the Doping

Next, we discuss the influence of the smoothness of the doping on the convergence order for the different discretization methods. Whenever we compare a coarse discrete solution (of size $2h$) to a finer one (of size h), we restrict the finer solution to the coarser mesh. Then we can subtract $\mathbf{u}^h$ from $\mathbf{u}^{2h}$ and slightly abusing the notation write $\|\mathbf{u}^h - \mathbf{u}^{2h}\|$ for the corresponding norm. Provided that the doping is sufficiently smooth and the carrier densities converge sufficiently fast, then the FV discretization of the Poisson equation is second order accurate, see the convergence for n, p, ψ in the top right panel of Fig. 3. When the doping is discontinuous ($\kappa = 5 \cdot 10^5$), the bottom row in Fig. 3 shows that also the convergence order of the FV electrostatic potential becomes linear, which is plausible by standard FE error estimates. From Fig. 3 it appears that while the error in the FE method is dominated by the quasi-Fermi potentials, the error in the FV method is dominated by the lack of regularity in the doping.

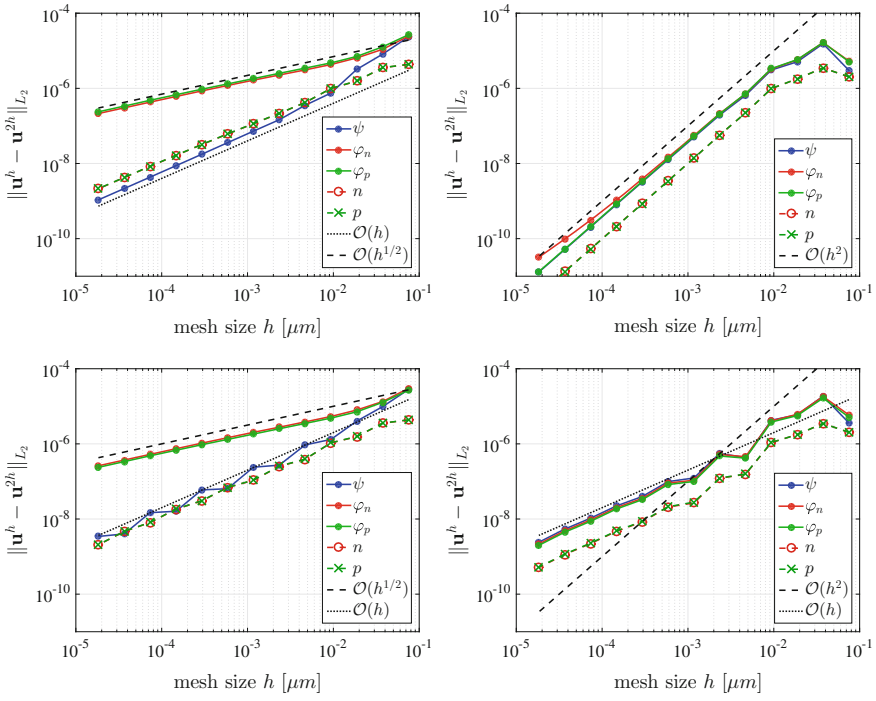

Fig. 3 L_2 convergence rates in 1D for solution (left) of the FE discretization and (right) of the FV discretization with $\kappa = 500$ in the top row and for $\kappa = 5 \cdot 10^5$ in the bottom row at $V_{\text{ext}} = 3\,\text{V}$

4.3 Corner Singularities and Boundary Adapted Meshes

Semiconductor devices may often be angular-shaped. However, in particular L-shaped domains pose numerical difficulties which we would like to study for the FE and FV methods. We consider a two-dimensional L-shaped domain

$$\Omega = [0, 2L]^2 \setminus [0, L]^2 \subset \mathbb{R}^2, \tag{7}$$

and impose ohmic contacts at the boundaries $(x, 0)$ and $(0, y)$ for $L \leq x, y \leq 2L$. All other boundaries are supplied with homogeneous Neumann boundary conditions. The p-i-n doping concentration $C : \Omega \to \mathbb{R}$ is given by

$$C(\mathbf{x}) = \begin{cases} +C_0 & 0 \leq x \leq L/2, \\ -C_0 & 0 \leq y \leq L/2, \\ +2C_0(L-x)/L & L/2 < x \leq L, \\ -2C_0(L-y)/L & L/2 < y \leq L, \\ 0 & \text{otherwise} \end{cases} \tag{8}$$

with $\mathbf{x} = (x, y)$ and as before $L = 10^{-7}m = 0.1\mu\text{m}$ and $C_0 = C_\text{m} = 10^{23}\,\text{m}^{-3}$. With this choice we ensure that the convergence order does not suffer from the regularity of the doping. However, constructing a non-convex domain with a corner angle $\vartheta = \theta\pi$ and $\theta = 3/2$ imposes a corner singularity of the form $\psi(\mathbf{x}) \sim r^{1/\theta}$ as $r \to 0$ for $r = \sqrt{(x - x_0)^2 + (y - y_0)^2}$ at $x_0 = y_0 = 0.1\mu\text{m}$.

The upper left panel of Fig. 4 shows the convergence of the electron quasi-Fermi potentials at $V_\text{ext} = 3\,\text{V}$, where the FE and FV are compared on a sequence of uniform and a sequence of boundary adapted meshes. As in 1D, the FV method converges quadratically. Furthermore, for the FV discretization the error seems not to be influenced very much by the boundary adapted meshes. In contrast, the FE method again has a lower convergence order and local adaptivity improves the L_2 error of the solution by about one order of magnitude.

The lower panels of Fig. 4 show the solutions at $V_\text{ext} = 0.2\,\text{V}$, where the boundary layer is moderate and solutions are closer to thermal equilibrium. Hence, the lower left panel shows the general tendency to have lower errors. However, the convergence is slower with an order between $\mathcal{O}(h)$ and $\mathcal{O}(h^{4/3})$, indicating a stronger influence of the corner singularity. This effect is even more pronounced in the lower right panel, in which for all the used methods the convergence of the electrostatic potential nicely follows the $\mathcal{O}(h^{4/3})$ order predicted by the error analysis of the corner singularity.

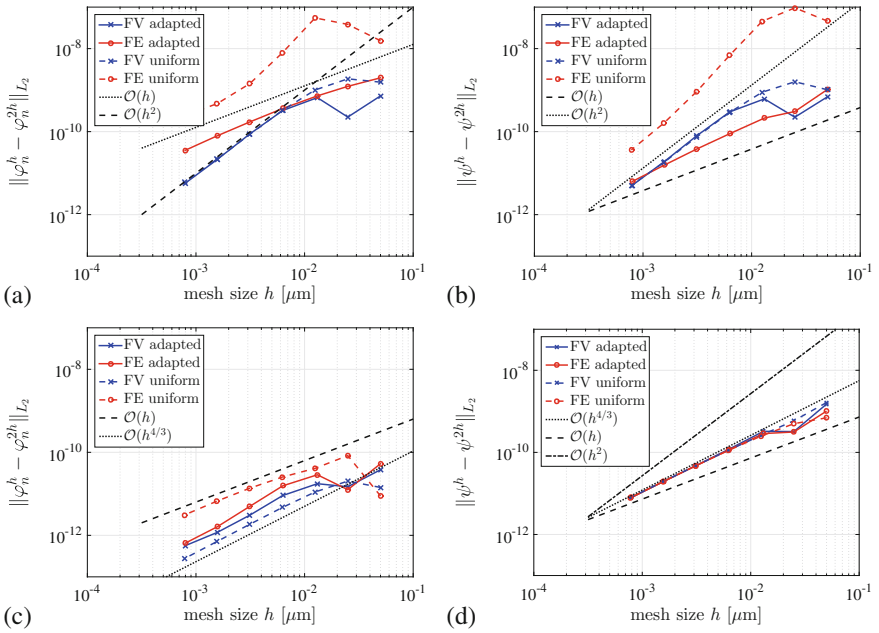

Fig. 4 Convergence of solutions on different meshes as a function of relative triangle size $h = 2^{-\ell}$ for **a** electron quasi-Fermi potential φ_n at $V_{\text{ext}} = 3\,\text{V}$, **b** electrostatic potential ψ at $V_{\text{ext}} = 3\,\text{V}$, **c** electron quasi-Fermi potential φ_n at $V_{\text{ext}} = 0.2\,\text{V}$, **d** electrostatic potential ψ at $V_{\text{ext}} = 0.2\,\text{V}$

5 Conclusion

Summarizing, in 2D both FE and FV discretizations deliver reasonable results. While the finite volume scheme often shows better convergence rates, the finite element method can be drastically improved by using meshes which are finer near ohmic contacts. We clearly observe that depending on the potential and the selected bias, the error is dominated by the boundary layer or the corner singularity. While the FV method generally handles the boundary layer well, the FE method in 2D introduces extra oscillations in the boundary layer, see [5] for details.

References

1. Bessemoulin-Chatard, M.: A finite volume scheme for convection-diffusion equations with nonlinear diffusion derived from the Scharfetter-Gummel scheme. Numer. Math. **121**(4), 637–670 (2012). https://doi.org/10.1007/s00211-012-0448-x
2. der Maur, MA., Povolotskyi, M., Sacconi, F., Pecchia, A., Romano, G., Penazzi, G., Di Carlo, A.: TiberCAD: towards multiscale simulation of optoelectronic devices. Opt. Quantum Electron. **40**(14-15), 1077–1083 (2008)

3. Eymard, R., Gallouët, T., Herbin, R.: Finite volume methods. In: Solution of Equation in $\mathbb{R}^n$ (Part 3), Techniques of Scientific Computing (Part 3), Handbook of Numerical Analysis, vol. 7, pp. 713 – 1018. Elsevier (2000)
4. Farrell, P., Rotundo, N., Doan, D.H., Kantner, M., Fuhrmann, J., Koprucki, T.: Mathematical methods: drift-diffusion models. In: J. Piprek (ed.) Handbook of Optoelectronic Device Modeling and Simulation, chap. 50, pp. 733–772. Taylor & Francis (2017)
5. Farrell, P., Peschka, D.: Nonlinear diffusion, boundary layers and nonsmoothness: analysis of challenges in drift-diffusion semiconductor simulations. Comput. Math. Appl. (2019). https://doi.org/10.1016/j.camwa.2019.06.007
6. Gajewski, H.: Analysis und Numerik von Ladungstransport in Halbleitern. WIAS Report (6) (1993). ISSN 0942-9077
7. Gärtner, K.: Existence of bounded discrete steady-state solutions of the Van Roosbroeck system on boundary conforming Delaunay grids. SIAM J. Sci. Comput. **31**(2), 1347–1362 (2009). https://doi.org/10.1137/070710950
8. van Mensfoort, S.L.M., Coehoorn, R.: Effect of Gaussian disorder on the voltage dependence of the current density in sandwich-type devices based on organic semiconductors. Phys. Rev. B **78**(8) (2008). https://doi.org/10.1103/physrevb.78.085207